Establishing Fluid Dynamics Scales Critical to Dynamic Interface Applications and their Impact on Handling Qualities

Quarterly Status Report 9

Period of Performance: 3/5/2023 – 6/4/2023

Prepared by:

G. R. Whitehouse
Continuum Dynamics, Inc.
34 Lexington Avenue
Ewing, NJ 08618-2302

Prepared for:

David Gonzalez
Office of Naval Research
875 North Randolph
Street
Arlington VA 22203

Under Contract No. N00014-21-C-1044

Glen R. Whitehouse

June 14, 2023

Project Summary

One of the most demanding tasks for naval aviators is landing on a moving flight deck in high sea-states (i.e. the dynamic interface (DI) problem - see Figure 1). This task is made even more difficult by aerodynamic disturbances at the landing spot from the flow around the ship's bow, superstructure and deck edges. This highly unsteady ship airwake can lead to significant pilot workload. Flight simulation has long been recognized as a valuable tool for augmenting engineering development and pilot training in DI operations, however, it is most effective when the underlying simulation model has appropriately characterized the complex aerodynamic interactions between the rotorcraft and ship airwake. Given the complexity of the problem, a fundamental difficulty when assessing the simulation approaches is the quantification of "good enough", both from the standpoint of understanding and predicting the underlying physics and also with regards to trainer fidelity (i.e. can the pilot feel/tell a difference). The premise of the proposed effort is to quantify "good enough" with regards to understanding the fundamental aero-physics of a rotorcraft interacting with an external disturbance field to quantify which length and time scales - such as those present in a ship airwake or in the wake of a an upstream aircraft during formation flight/refueling - directly impact the aircraft's fundamental response and flying qualities (FQ) along with the aeromechanics modeling fidelity required to simulate interactions adequately.

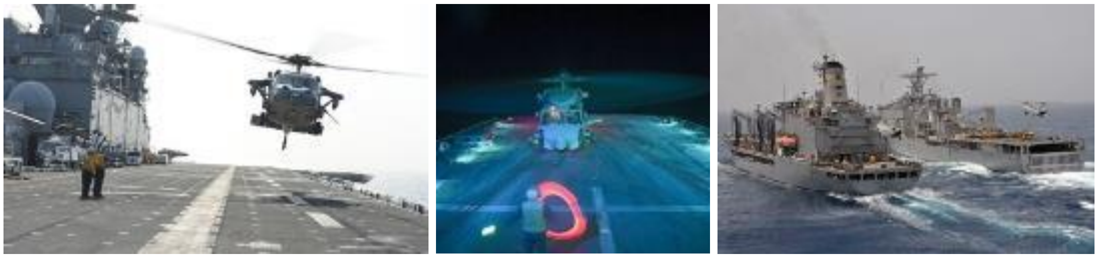

Figure 1: DI scenarios: landing on a moving deck (left), night operations (center) and approaching a pair ships (right)

Several ONR funded efforts that seek to quantify "good enough" have recently completed, or are underway, at the University of Maryland, Georgia Institute of Technology and NAVAIR, where the academic researchers are focusing on understanding the response of a wing to the wake shed by canonical structures [1] and the latter (Generalized Airwake Goodness Evaluation) program seeks to represent the entire DI scenario with a variety of methods. This effort does not seek to duplicate that work, rather to complement it by focusing on several fundamental unknowns in the rotorcraft community, namely:

1. What spatial and temporal scales, present in a disturbance field, matter from Flight Dynamics (FD) and FQ standpoints? Beyond the obvious constraints (i.e. larger than a rotor radius and those that induce velocities larger than the wake induced velocity), how does a rotor respond to different size disturbances and how does the rotor type influence this? For example, in general, a rotor acts to filter the influence of a disturbance field, but the level of filtering will vary significantly between an articulated flexible rotor (H-60) and a gimballed stiff one (V-22). Moreover, rotors typically respond ~90^{o} out of phase of the disturbance, whereas fixed aerodynamic surfaces response directly in-phase, which results in a fundamentally different response between rotorcraft types (i.e. helicopter vs. tiltrotor).

2. How do these scales vary when the effects on the full aircraft are accounted for? The primary response from the helicopter will be dominated by that of the rotor, though there may still be significant response associated with the disturbance induced flow on the fuselage, empennage and tail rotor.
3. How do these scales vary with aircraft configuration/type (i.e. conventional helicopter vs. tiltrotor)? The primary response from the helicopter will be dominated by that of the rotor, whereas the tiltrotor may respond primarily in a fixed wing manner associated with the induced flow on the wing. Of course, the tiltrotor's response will also vary with nacelle angle, and it is well known that the V-22's response to wake disturbances (i.e. during formation flight) is quite different to other rotorcraft in the Navy's inventory [2].
4. How do these scales vary with aircraft flight condition, and can valid modeling simplifications be made (i.e. distorting vs. classical frozen disturbance field)? Work by Whitehouse and Brown for helicopter rotors [3-7] suggests that for high speed flight, the traditional frozen field (superposition) assumption may be adequate, but that at the low speeds associated with DI operations, a distorting disturbance field and wake are required because the response is critically different.

Developing an understanding of fundamental aircraft aeromechanic response, FD, and FQ to the unknowns outlined above would provide great utility to the community with regards to establishing the level of modeling fidelity required to accurately simulate disturbance interactions, the level of fidelity required to be output by CFD simulation generated ship airwake databases for training scenarios, and the quantification and specification of handling qualities to types of disturbance fields that can be used to define future and ongoing training and aircraft performance requirements and specifications, such as ADS-33 [8].

Technical Objectives

The goal of the effort is to develop a fundamental understanding of the relationship between the length and time scales typically present in disturbance fields experienced by Naval aviators (i.e. ship airwakes, wing wakes etc.) and rotorcraft FD and FQ when the fully-interacting fluid dynamics of the airwake and rotor wake and flight mechanics are accounted for. With this information in hand, the engineering community would be better able to understand the relationship between aircraft type, ride quality, FD and FQ during flight conditions where disturbance fields are encountered. The community would be able to more accurately define trainer requirements, minimum experimental campaign requirements, minimum CFD modeling requirements and consequently establish a benchmark to evaluate CFD predictive capability. Furthermore, the conclusions of this work would also directly impact the development of requirements for new aircraft given the direct correlation between FD and FQ. The proposed effort would undertake the research required to develop such an understanding, with disseminating the observations and conclusions of the work to the Navy and the broader FD, FQ and handling qualities communities - a key objective from the outset. The effort will be structured using a build-up approach that first focuses on defining relevant disturbance fields followed by predicting and understanding the fundamental aeromechanics response (i.e. aerodynamic forces and moments and rotor dynamics). The effort would culminate in predicting the flight dynamics and handling qualities for realistic, but generic, helicopter and tiltrotor configurations that include representations of flight controls, propulsion system and crosscoupling characteristics. The key objectives for the effort roughly form the main tasks and are as follows:

1. Define the spatial and temporal fluid dynamic scales present in relevant disturbance fields and develop numerical representations for testing (Year 1).
2. 6-DOF generic model assembly and shakedown testing to ensure correct operation and functionality.(Year 1)
3. Define aeromechanics performance and HQ metrics along with a detailed simulation test matrix that includes systematic and consistent model fidelity build-up (Year 1-2).
4. Undertake simulation of a generic helicopter interacting with frozen and distorting disturbance fields to establish fundamental response characteristics (Year 2).
5. Undertake simulation of a generic tiltrotor interacting with frozen and distorting disturbance fields to establish fundamental response characteristics (Year 2).
6. Develop a realistic full helicopter model and undertake simulations of interactions with frozen and distorting disturbance fields to establish flight dynamics and handling qualities response (Year 3).
7. Develop a realistic full tiltrotor model and undertake simulations of interactions with frozen and distorting disturbance fields to establish flight dynamics and handling qualities response (Year 3).
8. Documentation and dissemination of observations and conclusions to the Navy and the wider FD/HQ community (Years 1-3).

Summary of Work Conducted During Reporting Period

Work during this reporting period focused on carrying out initial steps towards deriving/quantifying nondimensional scales to define the influence of various ship airwake features on rotorcraft fundamental response and testing the scalability of the set of nondimensional parameter relations introduced in previous progress reports. Analytical expressions for the influence of a generic flow structure on the response of an idealized rotor were derived using Blade Element Theory based analysis, which, in turn, can provide insights into scaling laws that could be applied.

Disturbance Model Testing

During this reporting period, the analytical arch vortex aft of a surface mounted obstacle in headwind flow was characterized and compared to CFD predictions. The model was quantified in terms of nondimensional position, size, and strength (circulation). We implemented a numerical vortex model to obtain predictions of airwake velocities associated with the arch vortex, representing the latter as a parabolic vortex filament with a ground mirror filament and using the Biot-Savart law combined with the Vatistas core model.

CFD Simulation

CFD simulations were performed using the CDI CGE/VorTran-M flow solver. CDI's adaptive cut-cell octree Cartesian Grid solver (CGE) is a Cartesian grid solver that solves the compressible URANS equations using either a Spalart-Allmaras (SA) or a shear stress transport (SST) turbulence model and resolves boundary layers and other highly anisotropic flow features in an efficient manner using wall functions. The VorTran-M model simulates the evolution of initial vorticity distributions in unbounded domains. The CGE/VorTran-M coupled arrangement consists of implementing the CGE solution on the grid as an “inner” solver that extends sufficiently far to contain regions with significant compressibility or flow turbulence and VorTran-M as an “outer” solver that is applied in the essentially incompressible flow region and efficiently transports the vorticity with minimal dissipation. Such an arrangement allows for computational savings in mesh resolution when compared to a solely CGE-based simulation. This coupled setup has been previously used for both ship and urban airwake modeling.

Flow feature characterization has focused on headwind flow over a simple cube to start off`. Primary flow features associated with a headwind flow over a cube are illustrated in Figure 2 and include

- A horseshoe vortex that forms upstream of the obstacle where the flow stagnates and wraps around the cube (feature “A” on the figure);
- On the top and side surfaces, local separation and reattachment regions (“B” and “C” on the figure);
- In the lee of the obstacle, an arch vortex (feature “D” on the figure) that forms due to the separation of the shear layers from the top and side surfaces. The streamlines aft of the obstacle indicate a recirculation region, where the direction of the flow reverses.

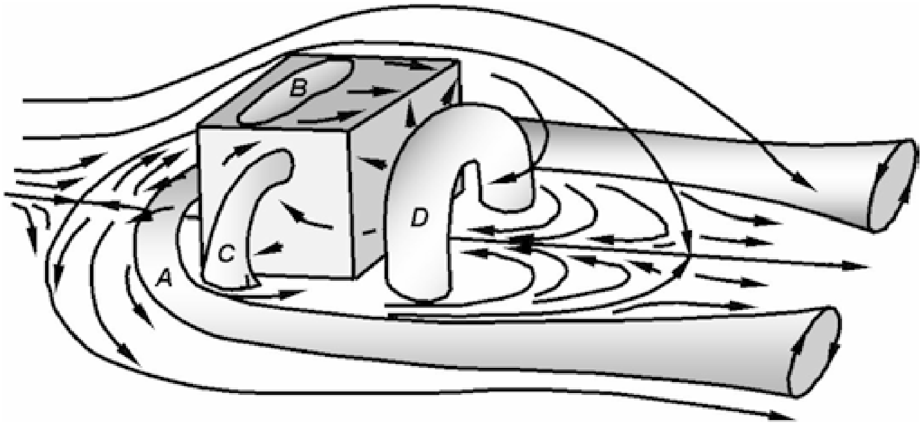

Figure 2: Schematic of principal flow features around surface-mounted obstacle [9].

CFD simulations were performed for a 30 m/s headwind over a 10 m cube. Although this speed is larger than would be typically encountered in practice, it is necessary to use a larger freestream velocity to maintain good numerical conditioning of the compressible flow solver. An alternative approach would have been to take advantage of the preconditioners implemented in CGE for low-speed flows. However, we deemed using the higher velocity appropriate given that the flow field is dominated by separation from the sharp edges of the cube, which has a weak dependence on viscosity. This further allowed us to perform simulations for inviscid flow only. Neglecting viscosity effects allows for scaling of time-accurate flow predictions using freestream velocity. This scaling has also been confirmed in viscous flow simulations for geometric configurations representative of the operating environments of rotorcraft. Note that no explicit atmospheric boundary layer (ABL) model was included in the simulation. Simulations were performed using a fixed time step of 0.005s. A steady CGE only simulation was first carried out to obtain a starting estimate for the transient coupled CGE/VorTran-M solution. This sequence enables an expedient solution that does not require the code to resolve and propagate the starting vortices far downstream, as would otherwise be expected from an impulsive start. In this reporting period, we used an updated CFD simulation where the transient simulation was carried out for duration of 40s, and where the first 15s were discarded as transition from steady to transient simulation and the subsequent 25 seconds worth of data were recorded for post-processing in 0.1s increments. Previously, we had used a 25s simulation where only the first 3s were discarded. We carried out this new simulation because had noted the presence of transients in velocity time-histories at certain discrete locations. Vortex shedding frequency is characterized by the Strouhal number, which is defined as

$$St = \frac{fb}{U} \tag{1}$$

where f is the vortex shedding frequency and b is the characteristic length. Results from literature indicate dominant periodicity for flow aft of a cube at a distance of 6H [10] to have a characteristic frequency of $St = 0.104$ [10, 11], where H is the cube height. Using 10 m cube length as characteristic length and the freestream velocity of 30 m/s as characteristic velocity, this Strouhal number corresponds to a vortex shedding frequency $f = 0.3$ Hz, which, in turn, corresponds to a period of 3.2 seconds. The trimmed 25 second simulation duration thus allows for approximately 8 cycles of vortex shedding to be captured. CFD results were compared to results from literature in previous progress reports.

We identified the flow features described previously in our simulations as well. This is illustrated in Figure 3, where we employ three two-dimensional (2D) planes to indicate the flow features. The right-handed coordinate system shown in Figure 3 has its origin at the center of the bottom face of the cube. Freestream is in the negative z direction. All position coordinates in this report are defined relative to this coordinate system unless stated otherwise.

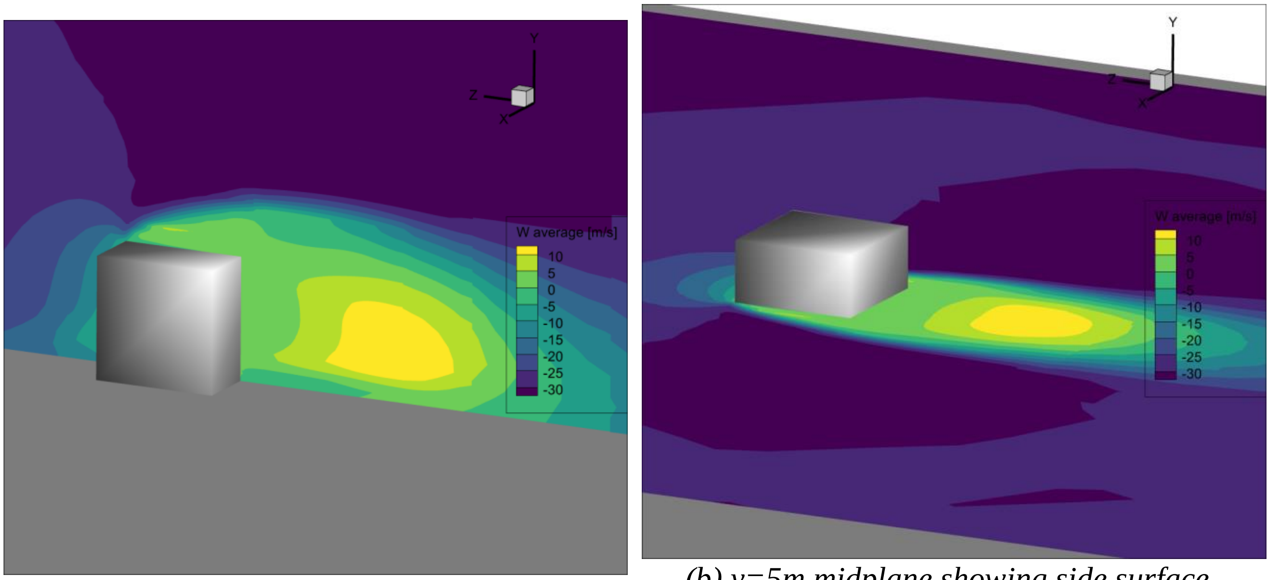

(a) x=0m midplane showing top surface separation and back step recirculation

(b) y=5m midplane showing side surface separation and symmetrical aft recirculation

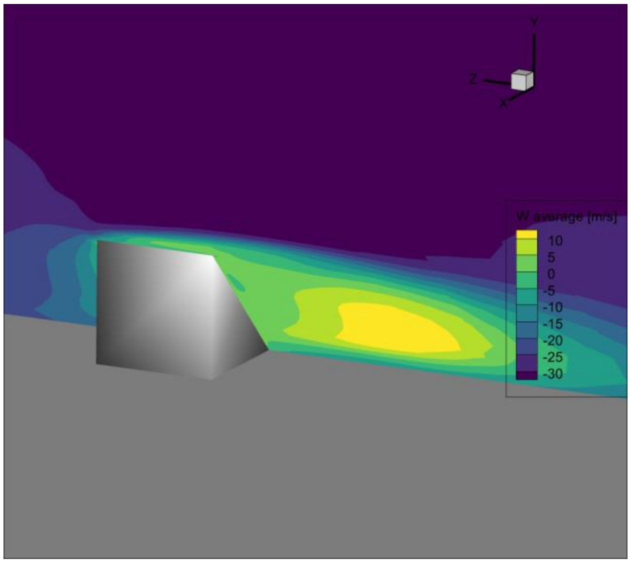

(c) diagonal plane that capture corner edge separation and aft recirculation

Figure 3: Contour of time-averaged longitudinal velocity for a 30m/s headwind simulation over a 10m cube using CGE/VorTran-M along planes containing primary flow features; center of coordinate system is at the center of the bottom face of the cube.

Flow Feature Characterization – Arch Vortex

Flow structures noted in Figure 2 are vortical structures that can be characterized in terms of their *geometry* (position and size) and *strength* (circulation). During the present reporting period, we carried out geometry and strength characterization for the arch vortex aft of the surface mounted cube with the goal of deriving an associated $v_{vortex}(r,\psi)$ function to employ with the expressions in Eq. (10). We employ a planar approach to the characterization, whereby we examine the time-averaged velocity, Q-criterion, and Δ-criterion distributions in various planes to identify (a) the center of the arch vortex, (b) the associated viscous core radius and (3) corresponding strength. Definitions for the Q- and Δ-criteria can be found in Ref. [12]. The planes we consider consist of the $x = 0$m midplane shown in Figure 3(a), and the $y = \{2.5, 3.5, 5, 7, 9\}$m planes. Figure 4 shows quiver plots of the velocity field across various $y =$ constant planes. The figure follows the general CGE/VorTran-M coordinate system described above. The aft recirculation zone is apparent with the blue "hole" near z=-20m. The arch vortex exists within the "white" region that bounds the hole on the Figure. The process we used in identifying the arch vortex center, size and strength consisted of:

1. Plotting the velocity field in the plane of interest as a quiver plot to locate vortex centers;
2. Ensuring any rotational behavior observed corresponded to a vortex by cross-checking with corresponding Q-criterion and Δ-criterion contour plots;
3. Picking out the vortex center position and the position where maximum tangential velocity is noted (the latter demarks the vortex core limit); and
4. Computing the circulation associated with the region that encloses the vortex.

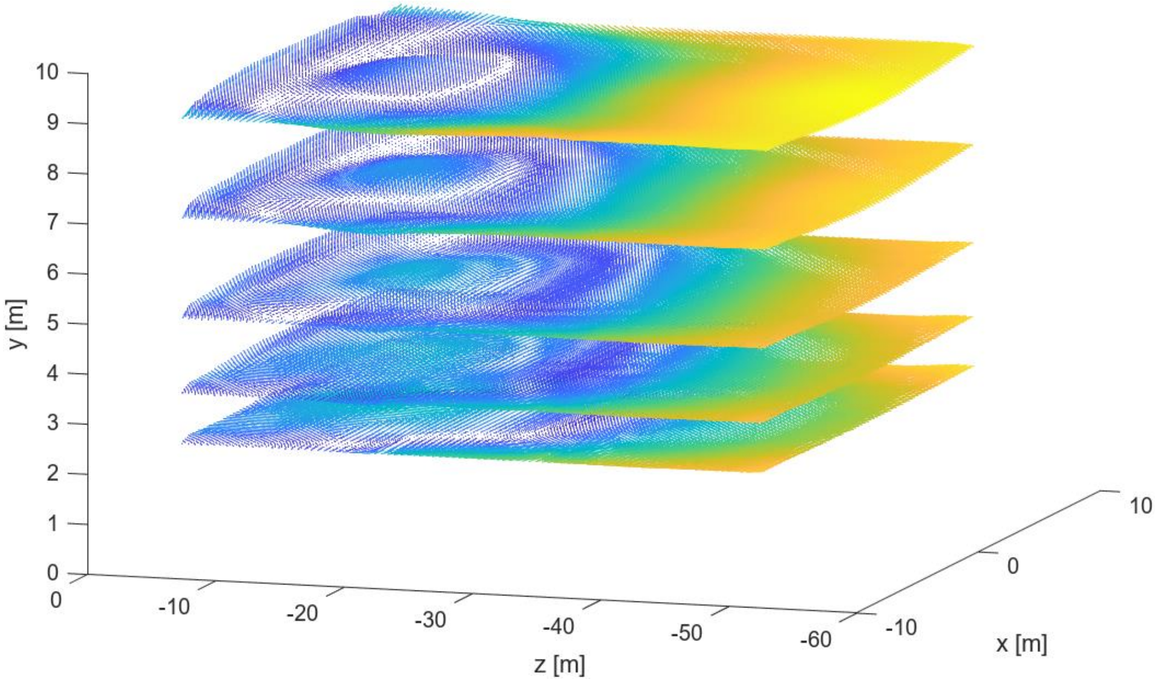

Figure 4: Quiver plot of in-plane velocity components at various heights; left to right along the z axis follows the flow downstream, down to up across the y axis goes upwards from ground.

We illustrate these steps using the y=5m plane. The quiver plot for time-averaged in-plane velocities is shown in Figure 5. From the figure, two vortices with centers at $[z, x] = [-15, -6.5]$m and $[z, x] = [-17, 6.5]$ m can be identified. Cross checking with the zoomed in Q- and Δ-criteria plots shown in Figure 6, we note that a vortex does indeed exist at $[z, x] = [-15, -6.5]$m. A stronger vortex exists near $x \approx -8.0m$, likely associated with the alternate vortices shed from the vertical edges of the cube. We assume symmetry exists and focus on this one confirmed vortex. It is important to crosscheck the centers identified from the quiver plots with those in Q- and Δ-criteria plots because, by themselves, quiver plots can fail to identify vortex cores depending on the reference frame relative to which they are plotted [13]. From the quiver plot in Figure 5, peak tangential (x) velocity along the z=-15m line (where the vortex center was identified) is noted at x=-0.5m, resulting in a vortex core radius size of

$$r_c = |-6.5 - (-0.5)| = 6\text{m}. \tag{2}$$

The final step consists of computing the vortex strength or circulation, which is defined as:

$$\Gamma = \oint_C \boldsymbol{v} \cdot d\boldsymbol{l} = \int_S (\nabla \times \mathbf{v}) \cdot d\boldsymbol{S} = \int_S \boldsymbol{\omega} \cdot d\boldsymbol{S}, \tag{3}$$

where $\boldsymbol{v}$ is the velocity field, d**l** is an infinitesimal length along a closed circuit C and $\boldsymbol{\omega}$ is the vorticity vector. Note that we apply Stokes theorem in Eq. (3) to convert the line integral to the surface integral. To compute the circulation, we first compute the out of plane vorticity by taking the curl of the planar velocities and then carry out a surface integral over the region bounded within $z \in [-13, -17]$m and $x \in [-8.5, -3.5]$m, a region selected from examining the Q- and Δ-criteria plots in Figure 6. This results in a circulation value of $\Gamma = 33.7\ \text{m}^2/s$.

We repeated the characterization procedure using various planes in the 3D space. Results are summarized in Table 1. Note that for the x=0m midplane shown in Figure 3(a), a secondary and more potent vortex exists further downstream at z=-21m, where part of the shear layer flows back into the recirculation zone while the other gets entrained downstream by freestream velocity.

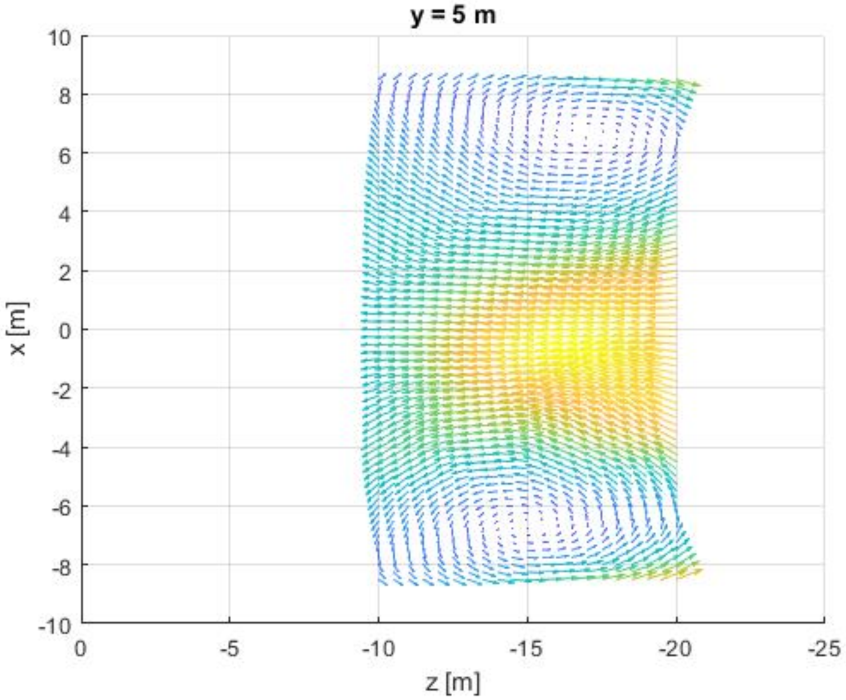

Figure 5: Quiver plot for y=5m plane.

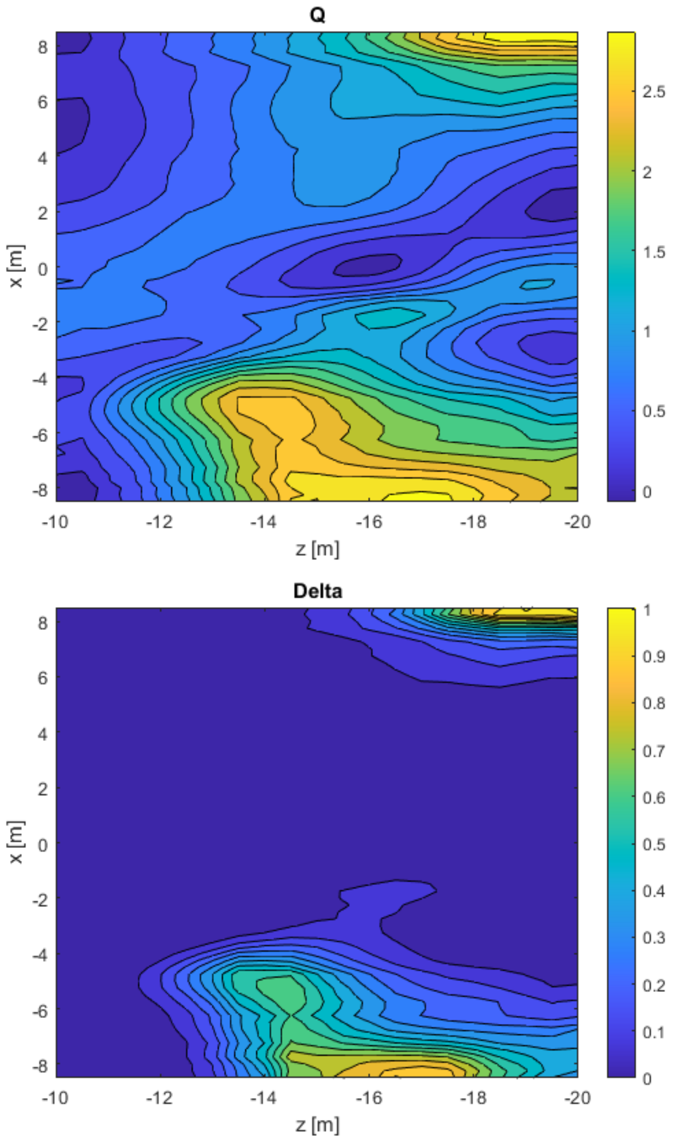

Figure 6: Q-criterion (top) and Δ-criterion (bottom) distributions for y=5m plane.

Table 1: Arch vortex characterization along different planes.

Plane	**Vortex #1 loc [m]**	**Radius [m]**	**Circ strength [m2/s]**
x=0m	$[z, y] = [-18, 12]$	1	26.5
y=9m	$[z, x] = [-16, -4.25]$	3.75	33.6
y=7.5m	$[z, x] = [-15, -5.5]$	4.5	33.1
y=5m	$[z, x] = [-15, -6.5]$	6	33.7
y=3.5m	$[z, x] = [-15, -7.5]$	7	31.5
y=2.5m	$[z, x] = [-16.5, -7.75]$	7.25	31.9

The arch vortex characterization information provided in Table 1 is specific to the headwind flow simulation over the 10m cube. We derived nondimensional relations using this information. The nondimensional position of the arch vortex center line is given by

$$\begin{aligned} \bar{y} &= 1.55\bar{x}^2 + 1.2, \\ \bar{z} &= -1.5H, \end{aligned} \tag{4}$$

where the coordinates $\bar{x}, \bar{y}$, and $\bar{z}$ have been nondimensionalized by obstacle width W, height H and length L, respectively. From Eq. (4), the arch vortex center is assumed to be a 2D parabola that exists in the $\bar{z} = -1.5H$ plane, see Figure 7.

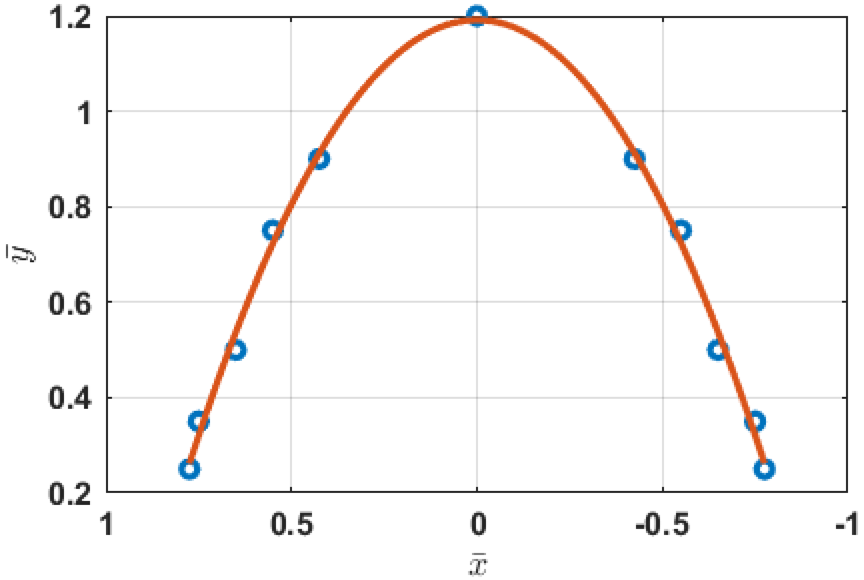

Figure 7: Parabolic representation of arch vortex in the $\bar{z} = -1.5H$ plane; blue points represent points from Table 1 and the red line represents the quadratic fit.

An expression for the nondimensional vortex core radius was similarly derived as a function of the nondimensional vertical coordinate $\bar{y}$:

$$\bar{r}_c = -0.90\bar{y} + 1.27. \tag{5}$$

From Table 1, the strength of the vortex in the different planes are close to each other, indicating viability of the vortex modeling approach. We averaged the corresponding values and nondimensionalized them using the freestream velocity magnitude of 30m/s and obstacle height $H = 10$m to obtain a nondimensional arch vortex strength of

$$\bar{\Gamma} = \frac{\Gamma}{U_\infty H} = \frac{31.7\ \mathrm{m}^2/s}{(30\ \mathrm{m/s})(10\ \mathrm{m})} = 0.106. \tag{6}$$

The applicability of the relations in Eqs. (4) to (6) for flow aft of obstacle of differing sizes is an aspect we will explore subsequently in the next reporting period. We represented the arch vortex as a parabolic vortex filament with a ground mirror counterpart and implemented a numerical vortex model that combined the Biot-Savart law with the Vatistas viscous core model [14] to obtain associated induced velocity predictions. The ground mirror filament helped satisfy Helmholtz theorem which states that a vortex filament must form a closed loop. The velocity induced by this arch vortex at a point located at position $\boldsymbol{r}$ relative to discretized vortex filament element $\boldsymbol{dl}$ was given by

$$\boldsymbol{V}_{ind} = \frac{\Gamma h}{4\pi(r_c^{2n} + h^{2n})^{1/n}} \int \frac{d\boldsymbol{l} \times \boldsymbol{r}}{|\boldsymbol{r}|^3} \times fac, \tag{7}$$

where h is the perpendicular distance of the evaluation point from the vortex filament element, n is an integer that controls the smoothness of the transition of the velocity predictions from the viscous core to the external inviscid region (we used $n = 1$), and fac is a scaling factor that varies with the nondimensional vertical coordinate $\bar{y}$ that we found necessary to include for accurate velocity magnitude predictions:

$$fac = -25\bar{y} + 25. \tag{8}$$

The induced velocities determined using Eq. (7), together with those from CGE/VorTran-M for the y = {2,4,6,8,10} m and x = {1,3,5,7,9} m planes for the 30m/s headwind flow over the 10m cube are plotted in Figure 8 and Figure 9, respectively. Note that the CGE/VorTran-M predictions include influence from all flow features whereas those of the vortex model only represent those from the arch vortex.

We make the following observations from the Figures:

a. For the y=constant planes, the lateral velocity U component predictions from the model exhibit similar magnitudes and spatial distributions as the CGE/VorTran-M predictions, while for the x=constant planes, the model prediction for U are similar to those from CGE/VorTran-M only in the x=5m and x=7m planes, with some discrepancies noted downstream in the z<-20m and y>10m regions.
b. For the y=constant planes, the model predicts an antisymmetric vertical velocity V distribution about z=-15m, which bears some resemblance to the predictions from CGE/VorTran-M but does not fully capture the expected velocities and magnitude, a mismatch which could be potentially improved by accounting for additional flow feature models. This mismatch is noted in the x=constant planes as well, although to a lesser extent, indicating the potential viability of the arch vortex model.
c. For both the y=constant and x=constant planes, peak longitudinal velocities W are adequately captured by the model in all planes except the y=10m plane. Additionally, the peak longitudinal velocity regions predicted by the model covers a smaller spatial domain than those from CGE/VorTran-M.
d. Predictions from the arch vortex model show reasonable agreement with expected velocities in the domain bounded approximately by $x \in [-5,5]$m, $y \in [2,9]$m and $z \in [-25, -10]$m, which corresponds to $\in [-W/2, W/2]$, $y \in [0.2,0.9]H$ and $z \in [0.5,2]H$ aft of the obstacle.

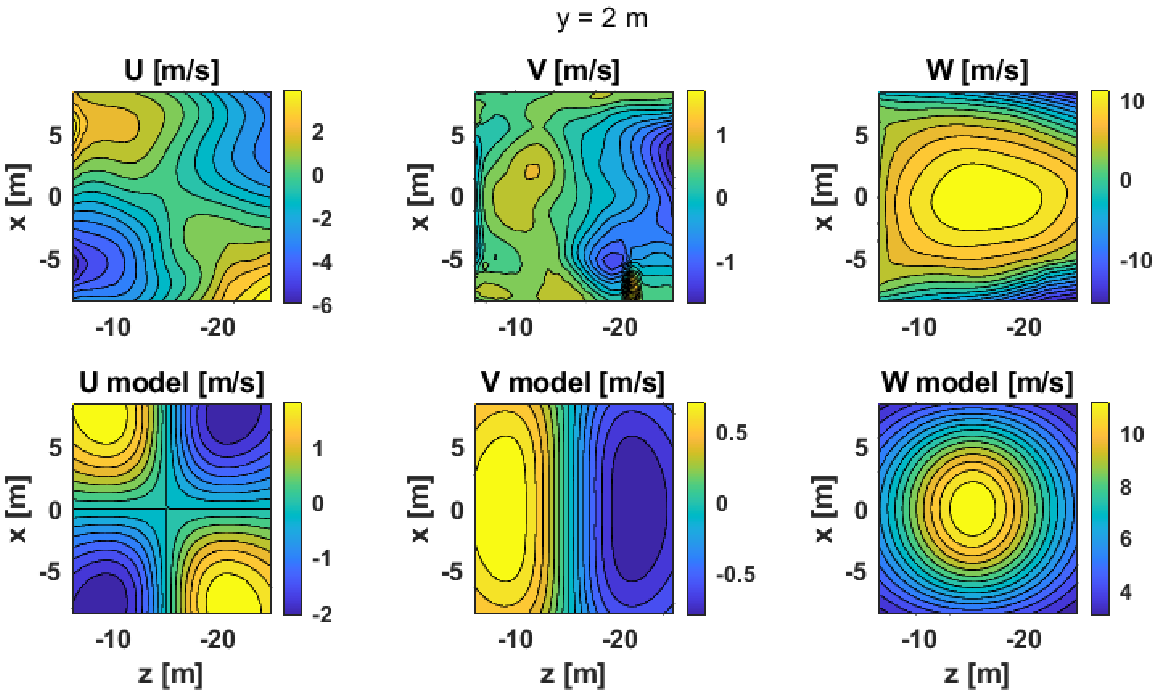
y = 2 m
U [m/s]
V [m/s]
W [m/s]
U model [m/s]
V model [m/s]
W model [m/s]
x [m]
z [m]
5
0
-5
-10
-20
2
0
-2
-4
-6
1
0
-1
10
0
-10
1
0
-1
-2
0.5
0
-0.5
10
8
6
4

(a)

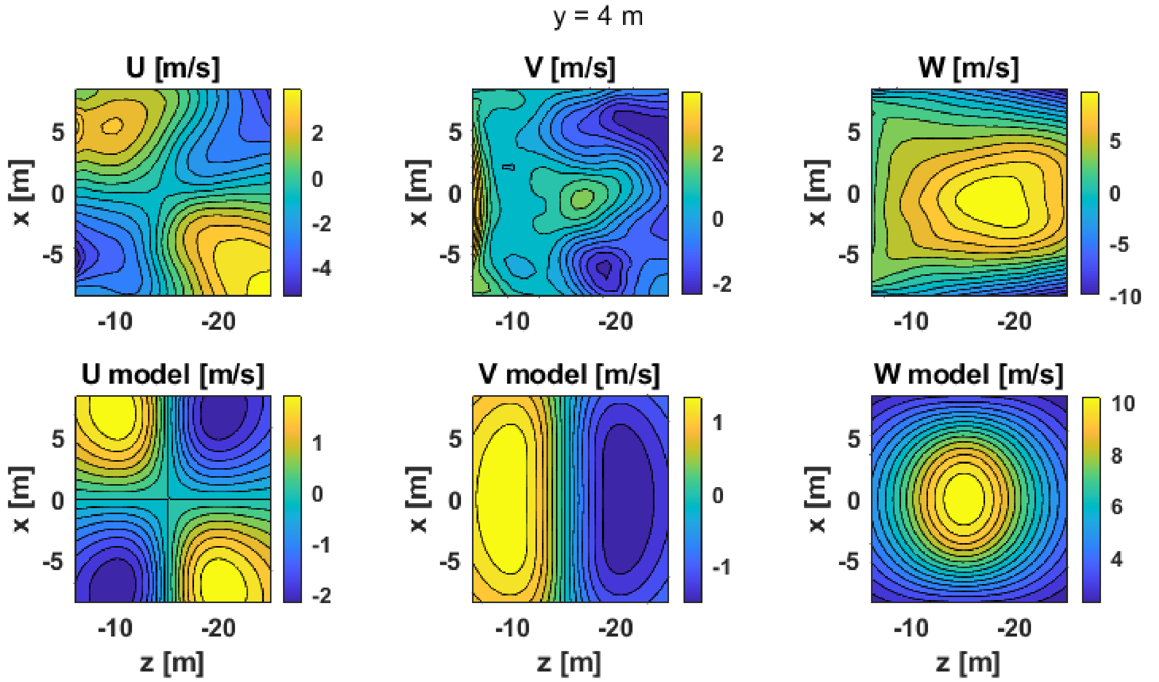
y = 4 m
U [m/s]
V [m/s]
W [m/s]
U model [m/s]
V model [m/s]
W model [m/s]
x [m]
z [m]
5
0
-5
-10
-20
2
0
-2
-4
2
0
-2
5
0
-5
-10
1
0
-1
-2
1
0
-1
10
8
6
4

(b)

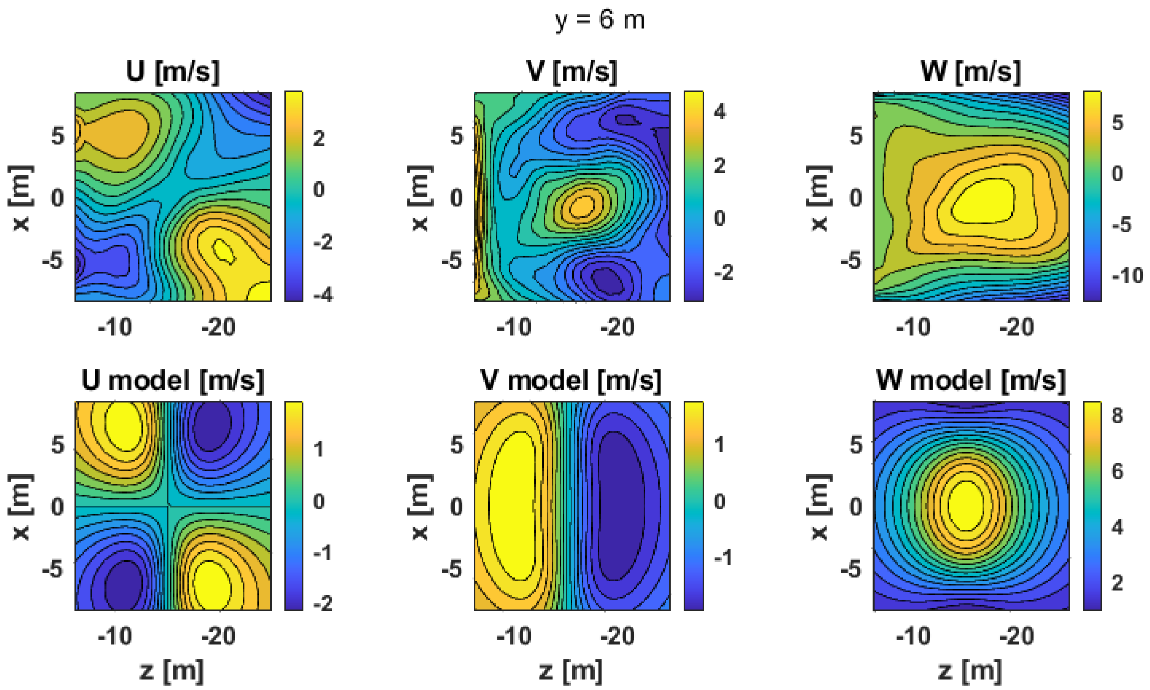
y = 6 m
U [m/s]
V [m/s]
W [m/s]
U model [m/s]
V model [m/s]
W model [m/s]
x [m]
z [m]
5
0
-5
-10
-20
2
0
-2
-4
4
1
-1
8
6

(c)

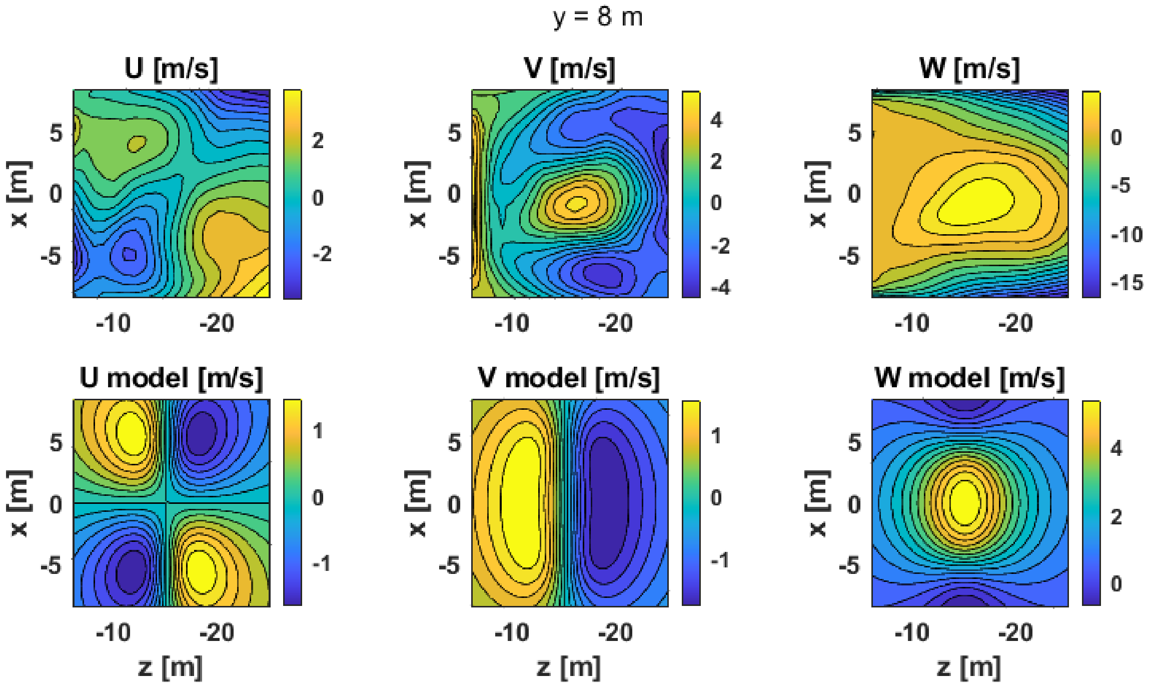
y = 8 m
U [m/s]
V [m/s]
W [m/s]
U model [m/s]
V model [m/s]
W model [m/s]
x [m]
z [m]
5
0
-5
-10
-15
-20
2
-2
4
-4
1
-1

(d)

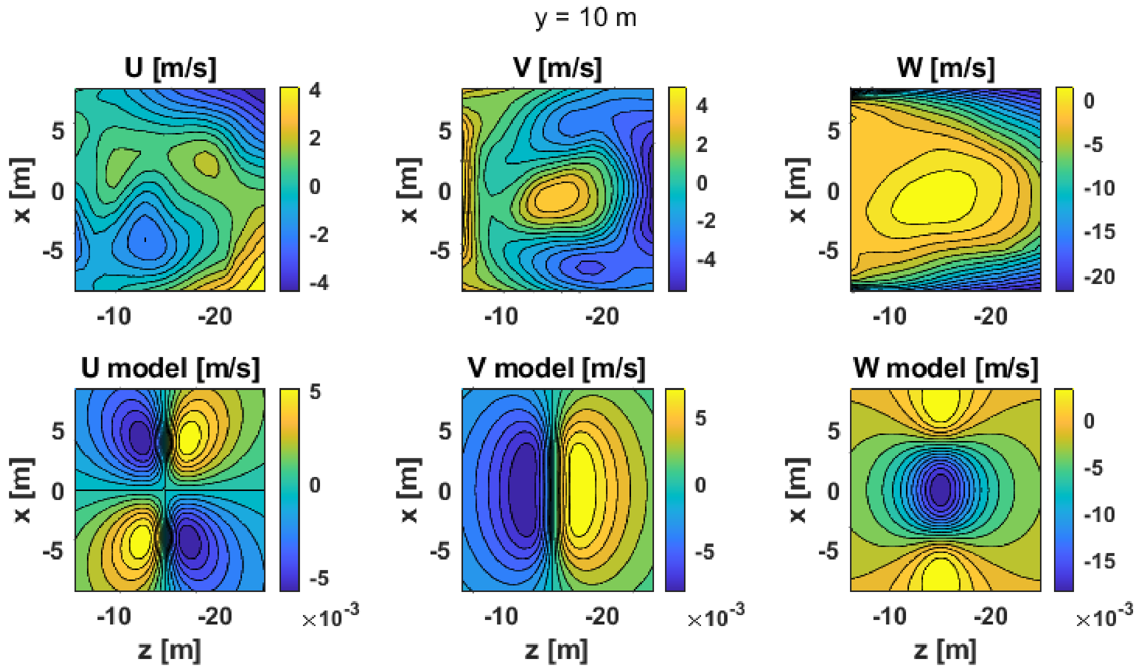

(e)

Figure 8: Contours of airwake velocity components aft of the 10m obstacle for various y=constant planes obtained using CGE/VorTran-M and arch vortex model.

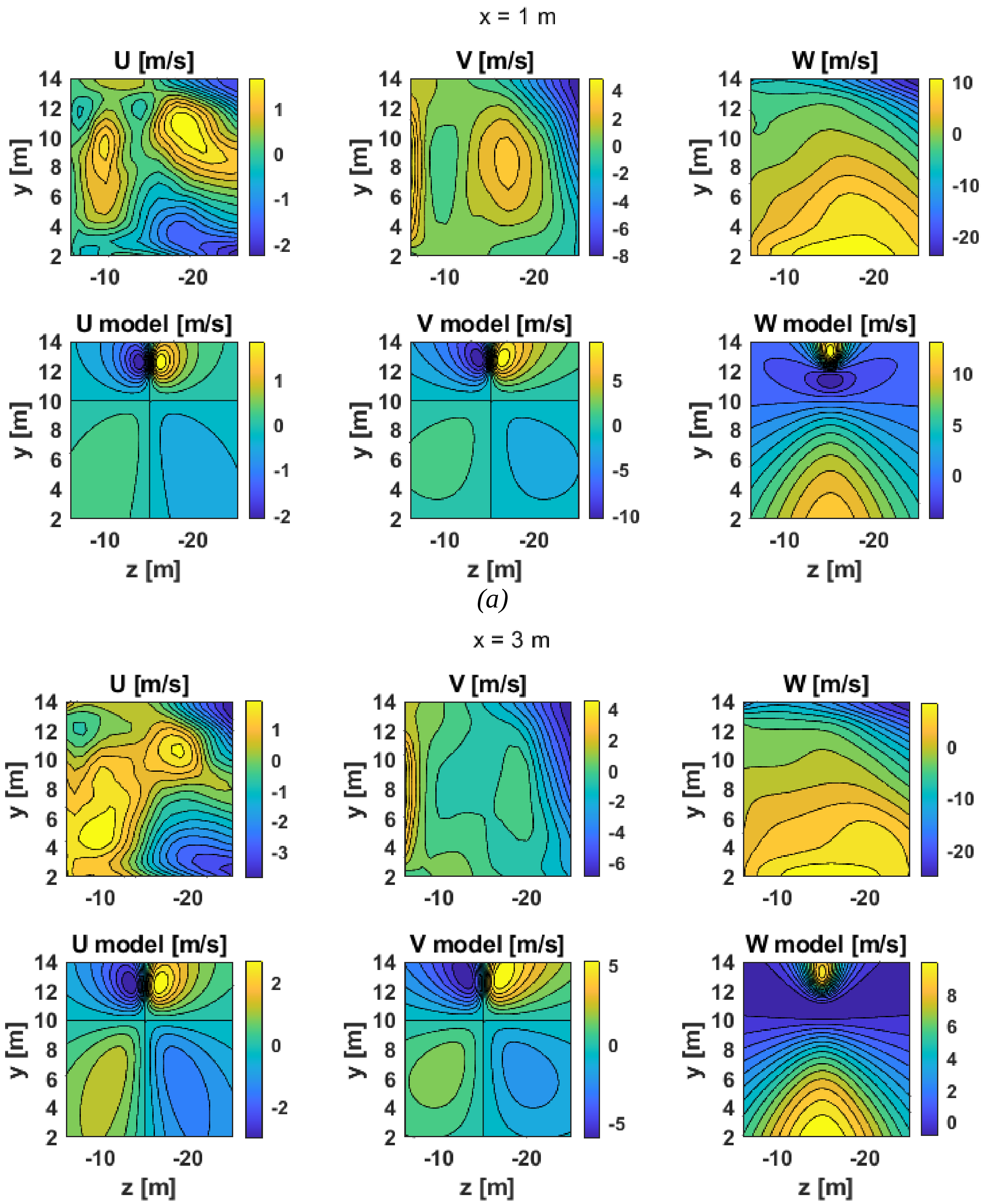
x = 1 m
U [m/s]
V [m/s]
W [m/s]
U model [m/s]
V model [m/s]
W model [m/s]
y [m]
z [m]
14
12
10
8
6
4
2
-10
-20
x = 3 m
U [m/s]
V [m/s]
W [m/s]
U model [m/s]
V model [m/s]
W model [m/s]

(a)

(b)

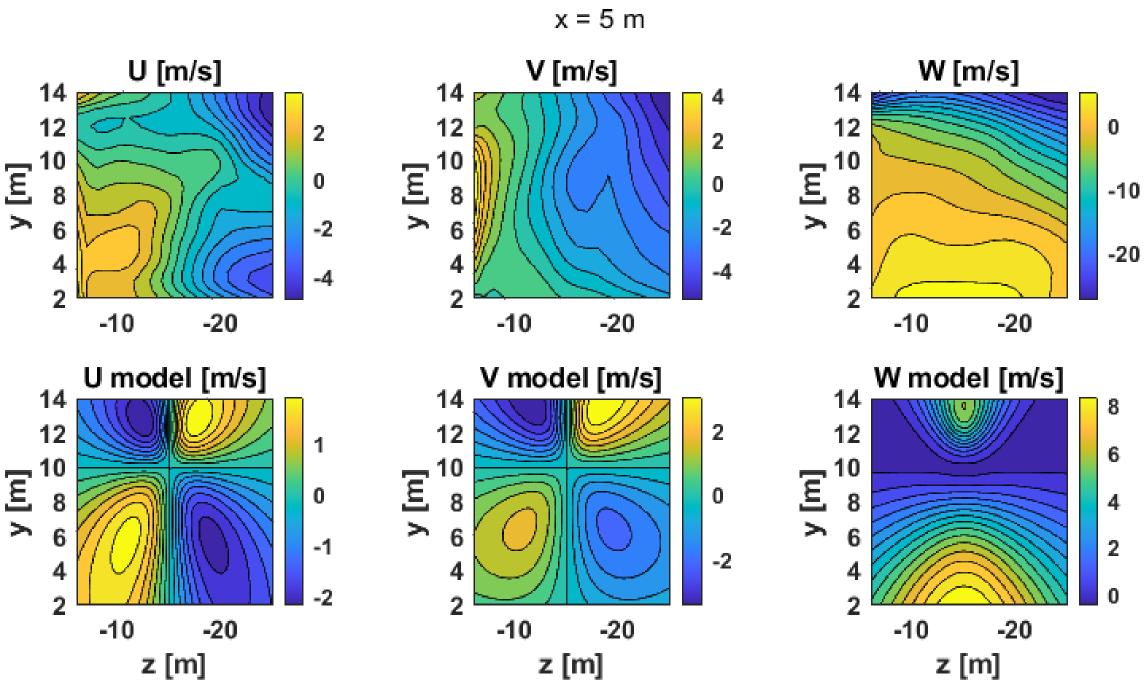
x = 5 m
U [m/s]
V [m/s]
W [m/s]
U model [m/s]
V model [m/s]
W model [m/s]
y [m]
z [m]
14
12
10
8
6
4
2
-10
-20
4
2
0
-2
-4
-10
-20
1
-1
8
6

(c)

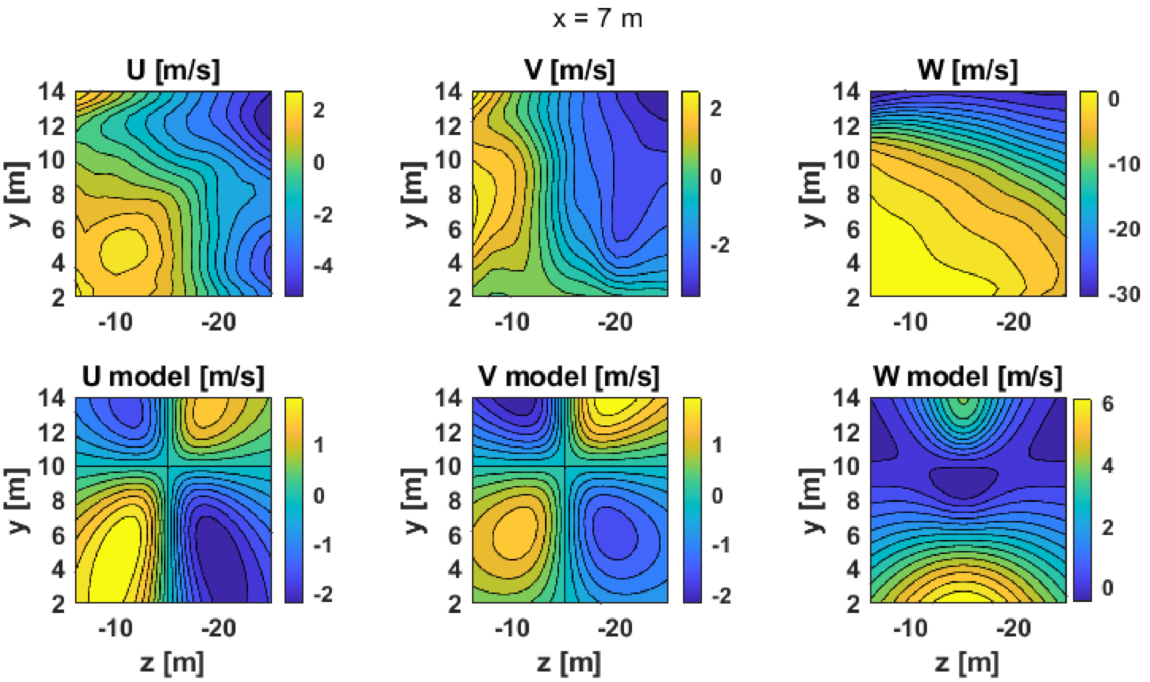
x = 7 m
U [m/s]
V [m/s]
W [m/s]
U model [m/s]
V model [m/s]
W model [m/s]
y [m]
z [m]
14
12
10
8
6
4
2
-10
-20
-30
2
0
-2
-4
1
-1
6

(d)

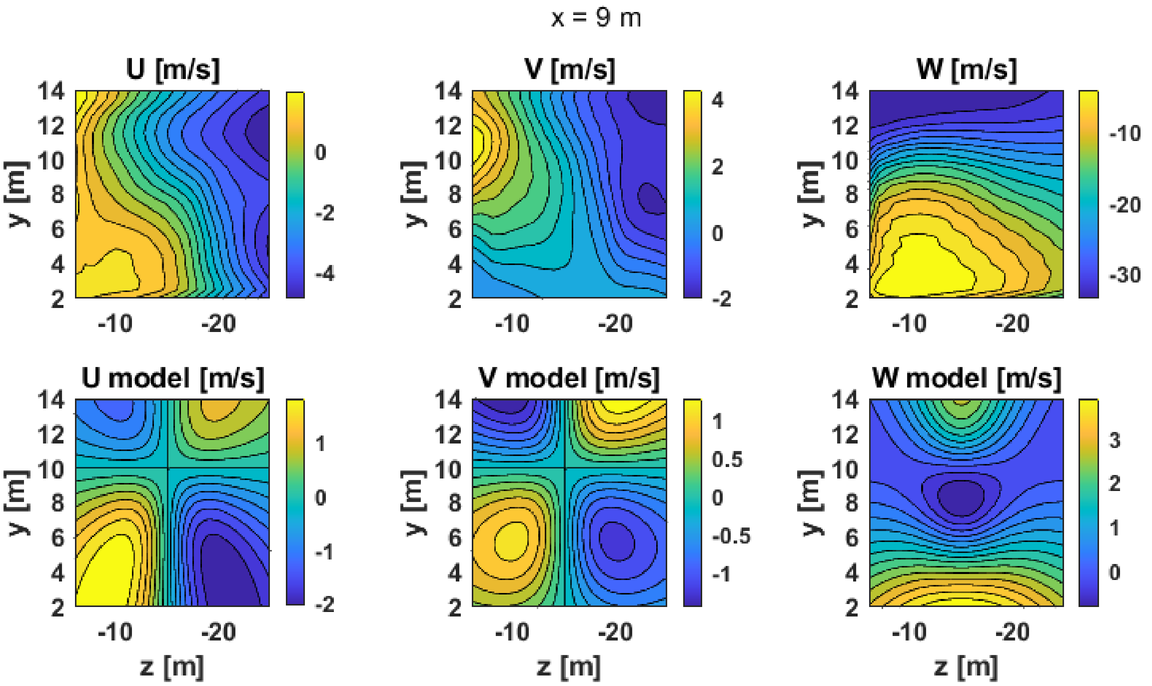

(e)

Figure 9: Contours of airwake velocity components aft of the 10m obstacle for various x=constant planes obtained using CGE/VorTran-M and arch vortex model.

Scaling Test for Time-Averaged Longitudinal Velocity Nondimensional Relations

In prior reports, we described analytical models capable of capturing time-averaged velocity profiles across various 2D planes. We demonstrated that representative 3D reconstruction of time-averaged velocity fields over the cube could be achieved from the 2D predictions. Inputs to the models were obtained using automated parameter fitting scripts. These inputs can be nondimensionalized and used as basis for scaling of the velocity profiles to arbitrary rectangular configurations. In the 7th report, we derived simplified nondimensional relations for the input parameters associated with longitudinal velocity aft of the cube that allowed us to adequately capture the corresponding velocity profile, whilst simultaneously providing a basis for scalability. During the present reporting period, we tested out the scalability of those relations by considering a 30 m/s headwind flow aft of a rectangular obstacle that is 10 m long, 30 m wide and 10 m high, where length, width and height are associated with the z, x and y axes shown in Figure 3, respectively.

The analytical longitudinal velocity model provides piece-wise functions to reconstruct the velocity profile across different regions. It derives from a vortex model introduced by Banks and Meroney [15] and can be thought of as a wheel being spun at two points: point M_{upper} at a velocity $U_{M_{upper}}$ and point M_{lower} at a velocity $U_{M_{lower}}$, see Figure 10.

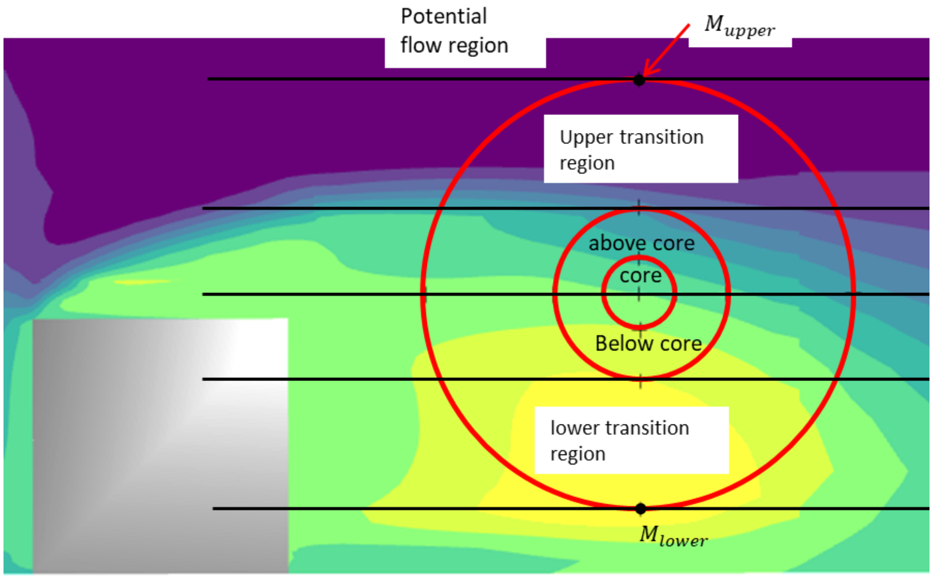

Figure 10: Illustration of modified Banks and Meroney vortex model shifted upwards.

Input parameters to model consist of:

1. location of vortex center (r_c).
2. vortex radius (h),
3. vortex core radius fraction (c)
4. location of point M_{upper} $(R_{M_{upper}})$,
5. location of point M_{upper} $(R_{M_{lower}})$,
6. velocity at point $R_{M_{upper}}$ $(U_{M_{upper}})$,
7. velocity at point $R_{M_{lower}}$ $(U_{M_{lower}})$,
8. location of point close to ground (r_0) below which the constant velocity was assumed, and
9. velocity near ground (U_0).

Sample longitudinal velocity predictions obtained using the model are given in Figure 11 for z=-18m along the mid plane shown in Figure 3(a).

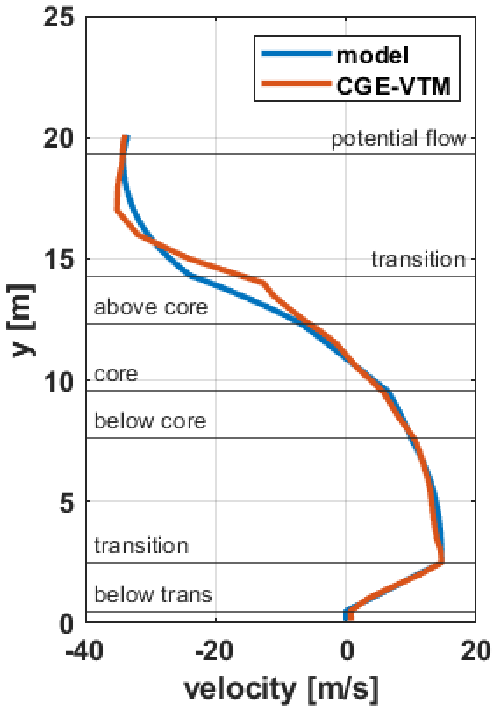

Figure 11: Longitudinal velocity profile along a vertical line through z=-18m in the lee of the cube obtained using the .

We derived nondimensional expressions for the model inputs by fitting polynomial functions on their spanwise variation along the x=0m midplane shown in Figure 3(a). Distance parameters $r_c, h, R_{M_{upper}},\ R_{M_{lower}}$ and r_0 were nondimensionalized using the obstacle height H while the velocity parameters $U_{M_{upper}}, U_{M_{lower}}$ and U_0 were nondimensionalized using freestream speed U_∞. The resulting expressions are provided next for reference.

$$\begin{aligned}
&\bar{r}_c(\bar{z}) = \ -0.07\bar{z}^2 + 0.081\bar{z} + 0.93,\\
&\bar{h}(\bar{z}) = 0.024\bar{z} + 0.28,\\
&\bar{c}(\bar{z}) = -0.17\bar{z} + 0.57,\\
&\bar{R}_{M_{upper}}(\bar{z}) = 1.56,\\
&\bar{R}_{M_{lower}}(\bar{z}) = 0.094\bar{z} + 0.14,\\
&\bar{U}_{M_{upper}}(\bar{z}) = 0.06\bar{z}^2 - 0.088\bar{z} - 1.15,\\
&\bar{U}_{M_{lower}}(\bar{z}) = -0.36\bar{z}^2 + 0.92\bar{z} - 0.13,\\
&\bar{r}_0(\bar{z}) = \ -0.0017\bar{z} + 0.015,\\
&\bar{U}_0 = -0.25.
\end{aligned} \tag{9}$$

By scaling expressions for distance parameters by obstacle width, and velocity expressions by freestream magnitude, we demonstrated that these relations could be employed to obtain longitudinal velocity predictions in the y=5m plane shown in Figure 3(b) as well. Similarly, if we dimensionalized the distance expressions by $L_C = 1.2L$, we could also recover representative velocity profiles along the diagonal plane shown in Figure 3(c).

Velocity predictions using the simplified relations along the transverse plane shown in Figure 12 are compared to CGE/VorTran-M predictions in Figure 13 for headwind flow over the 10m cube. The recirculation region represented by the model appears to be smaller than that predicted by CGE/VorTran-M, but the results are quite promising given the simplistic relations being employed.

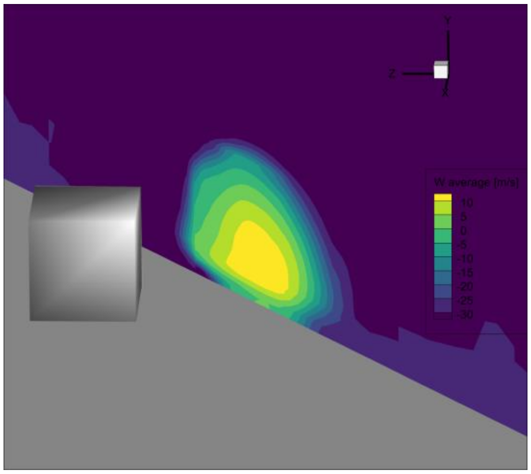

Figure 12: Transverse plane considered in parametric model evaluation.

During the present reporting period, we tested out the scalability of the relations given in Eq. (9) by considering a 30 m/s headwind flow over a rectangular obstacle that is 30 m wide, 10 m long and 10 m high. For this wider configuration, the recirculation region extends further downstream when compared to the cube but still exhibits similar longitudinal velocity profiles. We introduced constant x, y and z stretch factors that when employed with the relations given in Eq. (9), allowed us to obtain adequate velocity profiles. For instance, if we employ a constant z-coordinate stretch factor of 0.5, the velocity profiles predicted by Eq. (9) cover twice the longitudinal distance aft of the obstacle. By default, all stretch factors are 1. The stretch factors for the cuboid were determined manually by comparison with CGE/VorTran-M data, and one of the immediate tasks of in the next reporting period is to derive relations for these scaling factors by considering additional rectangular configurations.

Model predictions for a transverse plane similar to that shown in Figure 12 are shown in Figure 14 for the wider configuration. Despite the smaller size of the peak recirculation region predicted by the model, good agreement is noted with CGE/VorTran-M results. The larger size of the recirculation region is apparent in the contour plots.

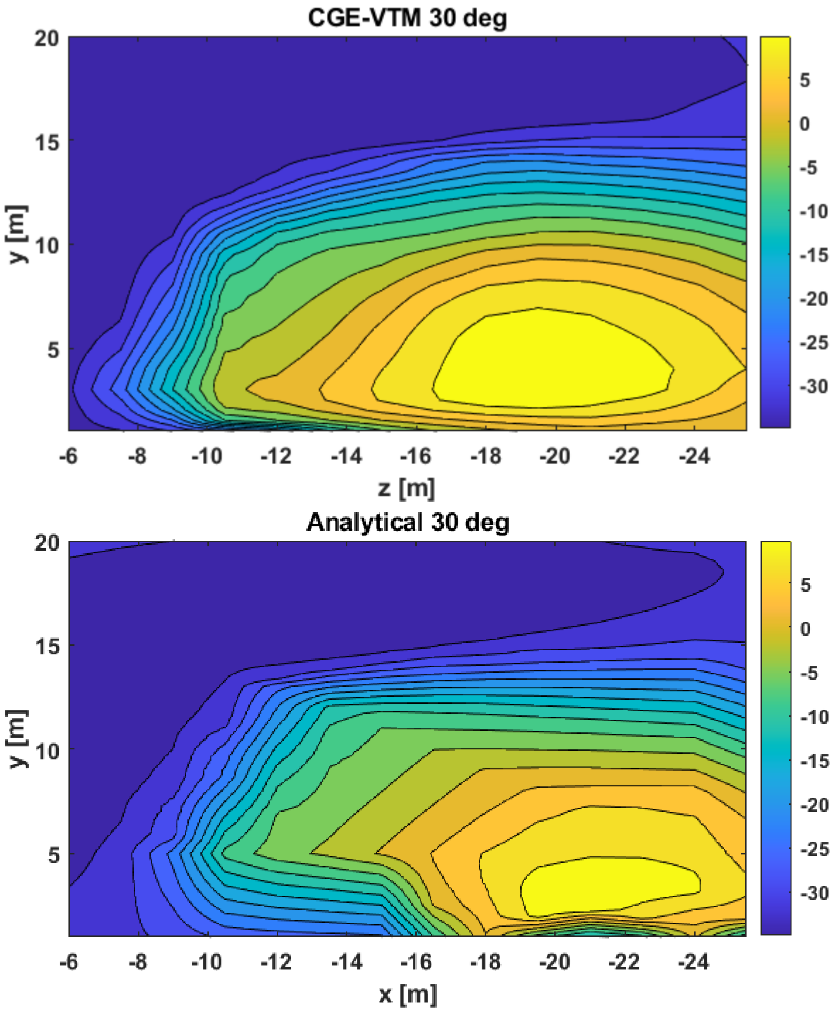

Figure 13: Mean longitudinal velocity contours along transverse plane aft of cube; truth (top) and parametric model (bottom).

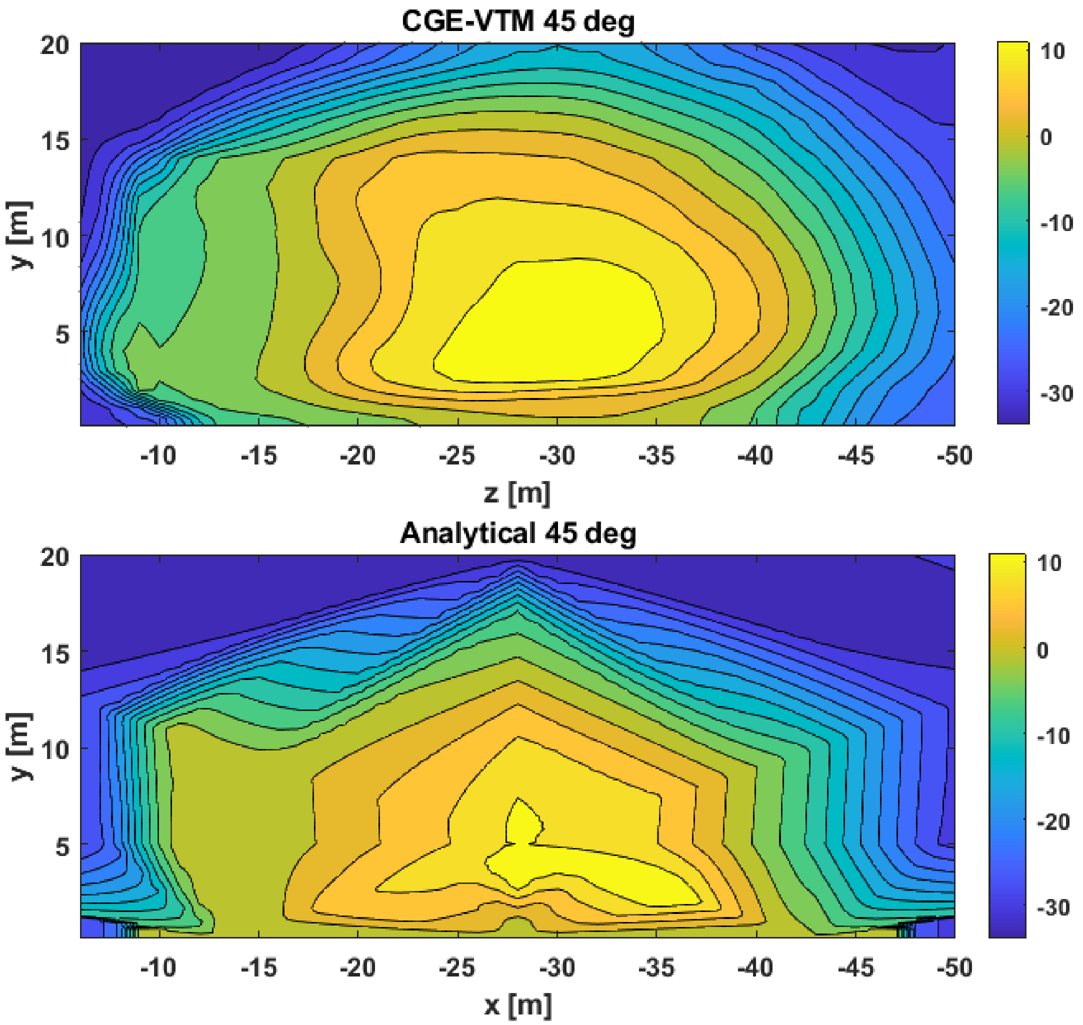
CGE-VTM 45 deg

Analytical 45 deg

Figure 14: Mean longitudinal velocity contours along transverse plane aft of 30m wide cuboid; truth (top) and parametric model (bottom).

Quantifying Fundamental Influence of Wake Structures on Rotorcraft

The influence of an arbitrary vortex wake structure on the fundamental response of a rotor can be derived using BET analysis [5, 7]. Detailed derivation of these equations is provided in Ref. [7]. We focus here on the assumptions made and resulting expressions.

Consider an “idealized” rotor with the following assumptions:

- No hub accelerations;
- Controls remain fixed;
- No hinge offset;
- Quasistatic response whereby the flap response of the rotor is much faster than the speed at which the vortex structure traverses the rotor; and
- Only the vertical component of the velocity associated with the arbitrary vortex is considered since it directly influences rotor inflow.

The influence of an arbitrary vortex with nondimensional vertical velocity $v_{vortex}(r,\psi)$, where r is the radial coordinate and ψ is the rotor azimuth, on rotor thrust coefficient C_T, coning β_0, lateral disc tilt β_{1s} and longitudinal disc tilt β_{1c} is given by the following expressions [7]:

$$C_T = C_T^* - \frac{Nca}{2\pi}\int_0^{2\pi}\int_0^R v_{vortex}(r,\psi)(r^2 + \mu\sin\psi)dr\,d\psi,$$

$$\beta_0 = \beta_0^* - \frac{ca}{4\pi^2\omega^2 I_\beta}\int_0^{2\pi}\int_0^R v_{vortex}(r,\psi)(r^2 + \mu r\sin\psi)dr\,d\psi, \tag{10}$$

$$\beta_{1s} = \beta_{1s}^* + \frac{ca}{2\pi^2(\omega^2-1)I_\beta}\int_0^{2\pi}\int_0^R v_{vortex}(r,\psi)(r^2\sin\psi + \mu r\sin^2\psi)dr\,d\psi,$$

$$\beta_{1c} = \beta_{1c}^* + \frac{ca}{2\pi^2(\omega^2-1)I_\beta}\int_0^{2\pi}\int_0^R v_{vortex}(r,\psi)(r^2\cos\psi + \mu r\cos\psi\sin\psi)dr\,d\psi,$$

where $(\ )^*$ terms represent the responses without the vortex, N is the number of rotor blades, a is the airfoil lift-curve slope, c is the blade chord length nondimensionalized by rotor radius R, ω is the flap natural frequency nondimensionalized by rotor rotational speed Ω ($\omega = 1$ for zero hinge offset), and I_β is the blade flapping inertia nondimensionalized by ρAR^3, where A is the rotor disc area. For a specified vortex velocity function $v_{vortex}(r,\psi)$, the corresponding influence on rotor fundamental response can therefore be quantified using the expressions in Eq. (10).

Rotor Fundamental Response

Earlier, we derived a velocity model for the arch vortex that develops aft of rectangular obstacles in headwind flow. This model is equivalent to the function $v_{vortex}(r,\psi)$ from Eq. (10) and enables the computation of fundamental rotor response to the airwake velocities associated with the arch vortex. For the fundamental response analysis, we consider rotors representative of four helicopters as summarized in Table 2. The expressions in Eq. (10) are evaluated using the rotor properties from Table 2 and the arch vortex model vertical velocity predictions obtained using Eq. (7). We consider two locations for the rotor hub center in our analyses: [x,y,z] = [0, 8, -20]m (location #1) and [x,y,z] = [0, 6, -25]m (location #2), both defined relative to the coordinate system shown in Figure 2.

Table 2: Rotor properties considered in fundamental response analysis.

Vehicle	**Number of blades**	**Chord [ft]**	**Radius [ft]**	**Rotation speed [rad/s]**	**GW [lbs]**	**Ibeta [slug-ft2]**
MQ-8C Fire scout (Bell 407)	4	0.9	17.5	43.25	5400	143.8
UH-60	4	1.73	26.83	27	16500	1512.6
V-22	3	2.09	19	41.57	39500	721.6
CH-53E	7	2.44	39.5	18.53	60000	6744.7

The intensity of the arch vortex influence on the different rotors is depicted in Figure 15 for hover ($\mu = 0$). Points that lie furthest from the origin indicate the strongest influence. At location #1, the influence of the arch vortex on the smaller MQ-8C rotor is strongest, followed in order of decreasing influence by the UH-60A rotor, the V-22 rotor and the CH-53E rotor. At location #2, the MQ-8C is again the most affected rotor, but this time, we note a greater arch vortex influence on the responses of UH-60A and CH-53E rotors. The influence of ship airwake flow features on rotor responses is thus characterized by both rotor properties (size, number of blades etc.) and position. Contours of velocity predictions using the arch vortex model and CGE/VorTran-M over the MQ-8C and CH-53E rotors (smallest and largest rotors considered, respectively) at locations #1 and #2 are shown in Figure 16 and Figure 17, respectively, for reference. Reasonable agreement in velocity predictions is noted with the largest discrepancies noted for the vertical velocity predictions, as was noted previously as well.

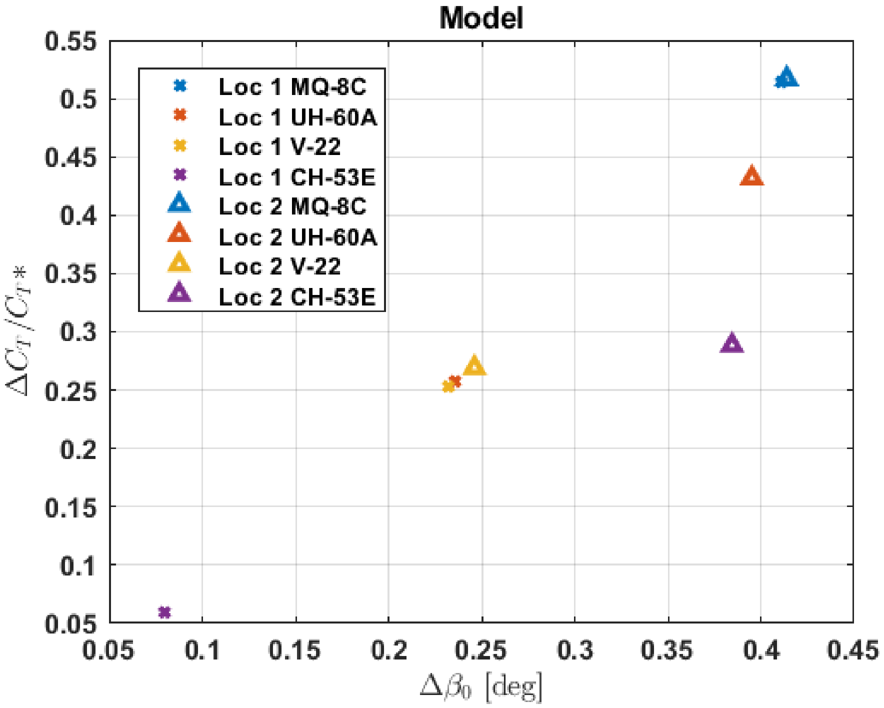

Figure 15: Influence of arch vortex on rotor fundamental response; $C_T^* = W/\rho(\pi R)^2(\Omega R)^2$, $\Delta C_T = C_T - C_T^*$, $\Delta\beta_0 = \beta_0 - \beta_0^*$.

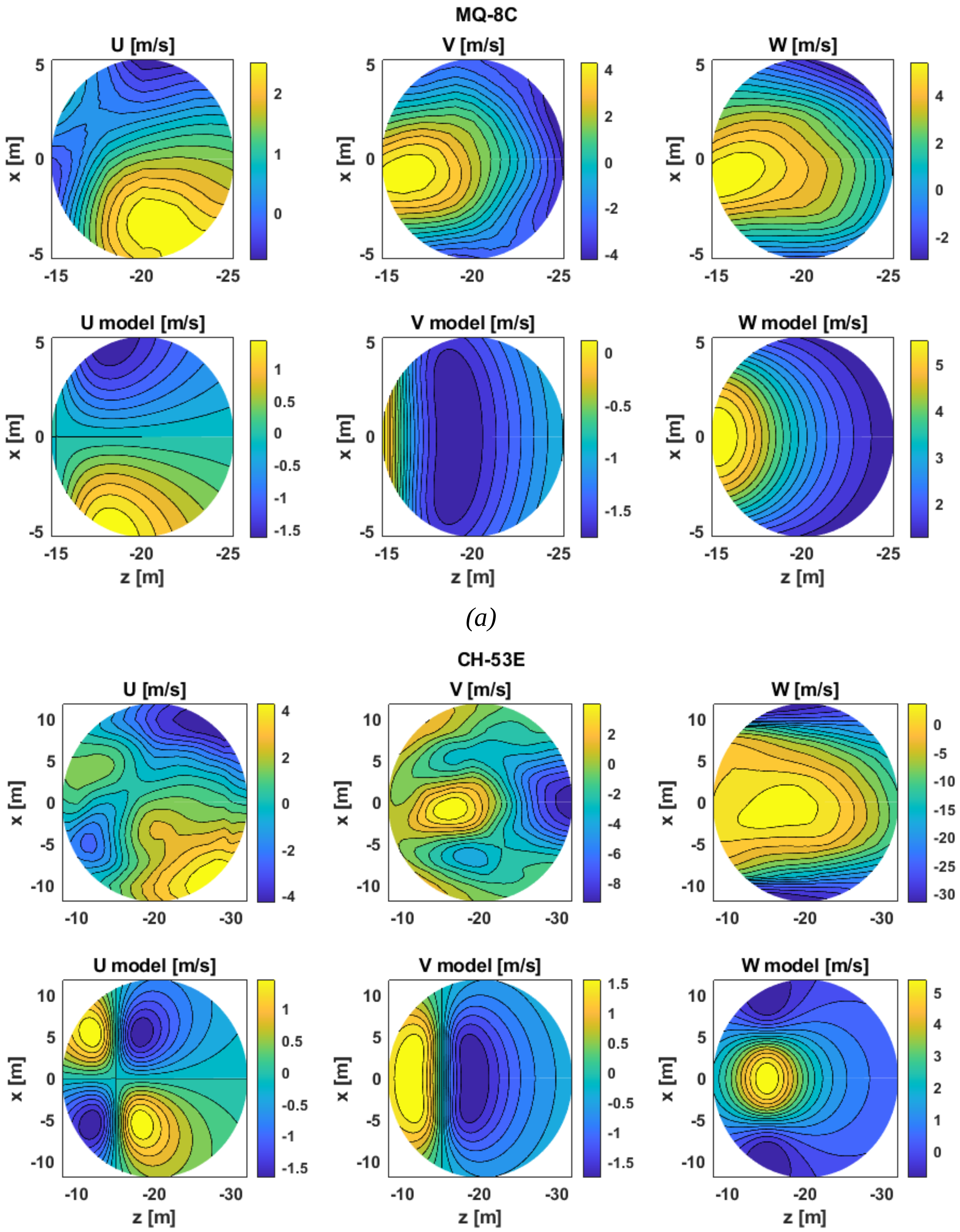

(a)

(b)

Figure 16: Contours of airwake velocity components over MQ-8C and CH-53E rotor centers at location #1 where [x,y,z] = [0, 8, -20]m.

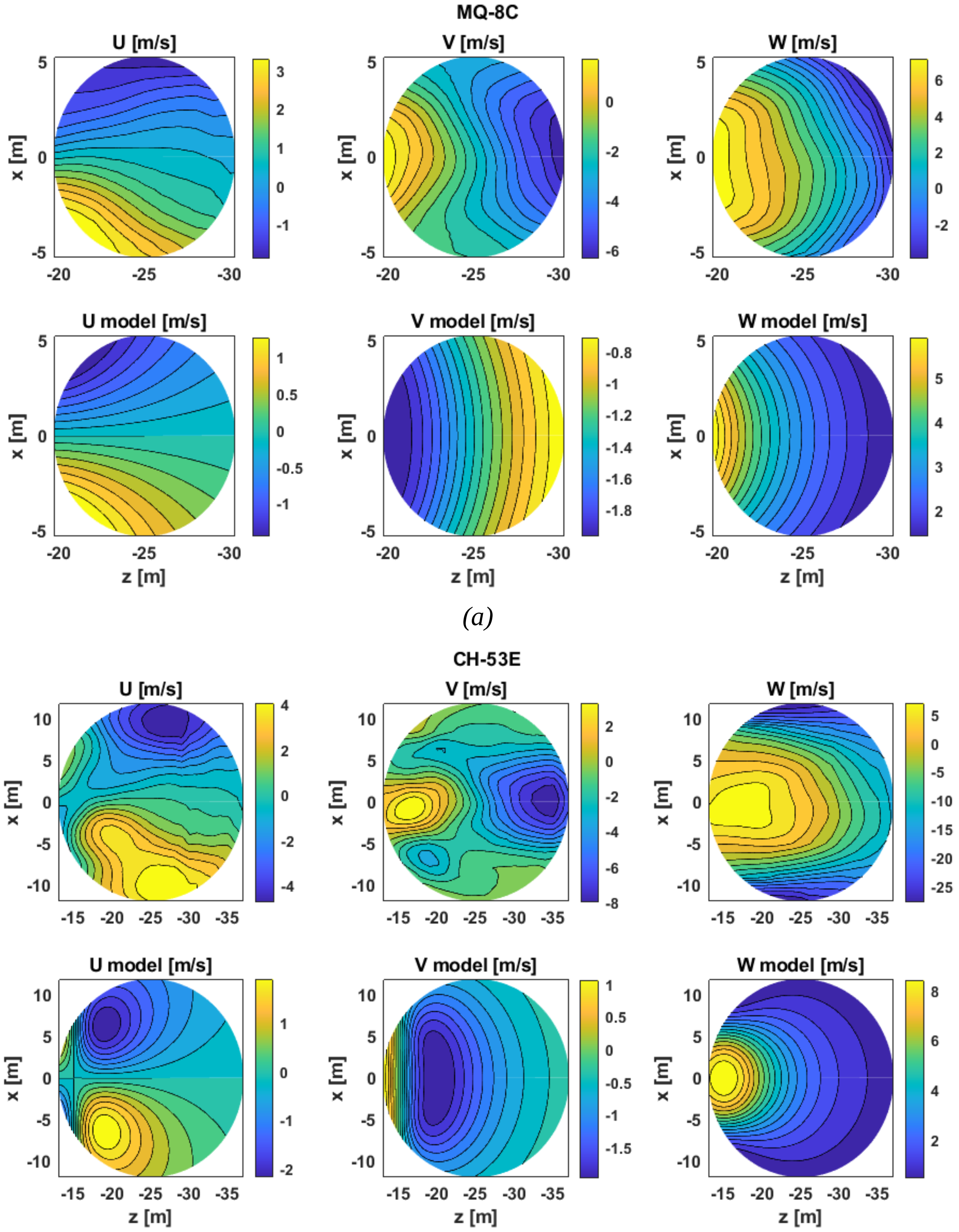

(a)

(b)

Figure 17: Contours of airwake velocity components over MQ-8C and CH-53E rotor centers at location #2 where [x,y,z] = [0, 6, -25]m.

Plans for the Next Reporting Period

In the next reporting period, we will build upon the understanding of the types of flowfields experienced by naval aviators described previously and continue to quantify the scales and nature of the relevant primary flow structures. Characterization of ship airwake flow features as vortical structures in terms of size and strength is an aspect that does not seem to have been examined in literature. In this reporting period, we performed such a characterization for the arch vortex noted aft of rectangular obstacles (representative of simplified ship superstructures) for headwind flow and subsequently performed a nondimensional analysis of its influence on the fundamental response of rotors representative of four different classes of rotorcraft, including the MQ-8C, UH-60A, V-22 and CH-53E. In the subsequent reporting period, we will perform similar characterization of additional ship airwake flow features and examine the viability of superposition to adequately represent airwake associated with different ship geometries. We will also consider aircraft response in terms of additional parametrizable and scalable metrics beyond aircraft fundamental response, and we will continue work on the development of scalable analytical models for full airwake reconstruction, including lateral and vertical velocity components. As mentioned in the prior report, CHARM has been fully integrated with CASTLE and the V-22 model. During the next period of performance we will complete integration with the Example Helicopter Model and confirm operation. Development of representative “canonical” surrogate flowfields will continue, and we will work on testing them out in CASTLE simulations.

References

1. Smith, M.J., et al. *Identification and Quantification of the Role of Turbulence in Aircraft/Ship Aerodynamics*. *ONR Annual Review*. 2020. Arlingon, VA.
2. Silva, M.J., et al. *The Role of Modeling & Simulation in the Mitigation of V-22 Tiltrotor Formation Flight Wake-Induced Roll-off*. *72nd Annual Forum of the American Helicopter Society*. 2016. West Palm Beach, FL.
3. Whitehouse, G.R. and R.E. Brown. *Modelling a Helicopter Rotor's Response to Encounters with Aircraft Wakes*. in *28th European Rotorcraft Forum*. 2002. Bristol, UK.
4. Whitehouse, G.R. and R.E. Brown. *Helicopter Rotor Response to Wake Encounters in Ground Effect*. in *59th Annual Forum of the American Helicopter Society*. 2003. Phoenix, AZ.
5. Whitehouse, G.R. and R.E. Brown, *Modelling the Mutual Distortions of Interacting Helicopter and Aircraft Wakes.* Journal of Aircraft, 2003. **Vol. 40**(No. 3): p. pp. 440-449.
6. Whitehouse, G.R. and R.E. Brown, *Modelling a Helicopter Rotor's Response to Wake Encounters.* The Aeronautical Journal, 2004. **Vol. 108**(No. 1079): p. pp. 15-26.
7. Whitehouse, G.R., *Helicopter Response to Vortex Encounters in the Near-Airfield Environment*, 2003, PhD Thesis, Department of Aeronautics Imperial College London.
8. ADS-33E-PRF. *Aeronautical Design Standard Performance Specification Handling Qualities Requirements for Military Rotorcraft*. in *US Army Aviation and Missile Command, Aviation Engineering Directorate*. 2000. Redstone Arsenal, Alabama.
9. Sousa, J.M.M., *Turbulent Flow Around a Surface-Mounted Obstacle Using 2D-3C DPIV.* Experiments in Fluids, 2002. **Vol. 33**(No. 6): p. pp. 854-862.
10. Yakhot, A., et al., *Turbulent Flow Around a Wall-Mounted Cube: A Direct Numerical Simulation.* International Journal of Heat and Fluid Flow, 2006. **Vol. 27**(No. 6): p. pp. 994-1009.

11. Klotz, L., et al., *Experimental Investigation of Flow Behind a Cube for Moderate Reynolds Numbers*. Journal of Fluid Mechanics, 2014. **Vol. 750**: p. pp. 73–98.
12. Haller, G., *An Objective Definition of A Vortex*. Journal of Fluid Mechanics, 2005. **Vol. 525**: p. pp. 1-26.
13. Jeong, J. and F. Hussain, *On The Identification of a Vortex*. Journal of Fluid Mechanics, 1995. **Vol. 285**: p. pp. 69-94.
14. Bagai, A. and J.G. Leishman, *Flow Visualization of Compressible Vortex Structures Using Density Gradient Techniques*. Experiments in Fluids, 1993. **Vol 15**(No. 6): p. pp. 431-442.
15. Banks, D. and R.N. Meroney, *A Model of Roof-Top Surface Pressures Produced by Conical Vortices: Model Development*. Wind and Structures, 2001. **Vol. 4**(No. 3): p. pp. 227–246.